Computational study of Li_3BO_3 and Li_3BN_2 I: Electrolyte properties of pure and doped crystals

Yan Li [1], Zachary D. Hood [2], and N. A. W. Holzwarth [1]
[1] *Department of Physics, Wake Forest University, Winston-Salem, North Carolina 27109, USA*
[2] *Applied Materials Division, Argonne National Laboratory, Argonne, Illinois 60439, USA*

(Received 22 June 2021; accepted 29 July 2021; published 17 August 2021)

Both Li_3BO_3 and Li_3BN_2 materials have promising properties for use in all-solid-state batteries and other technologies dependent on electrolytes with significant ionic conductivity. As the first of a two-part study, this paper reports the analysis of detailed simulations of Li ion diffusion in the monoclinic forms of these materials. Using both NEB and MD methods, it is clear that Li ion migration via vacancy mechanisms provides the most efficient ion transport in each material. While the results suggest that interstitial defects in these materials do not play a direct role in Li ion migration, their relative stability seems to enhance vacancy production via the formation of Frenkel-type defects. This may partially explain why the Li ion conductivities computed from MD simulations of samples initially containing a single Li ion vacancy are in reasonable agreement with measured values of this work for Li_3BO_3 and those reported in the literature for poorly crystalline samples of both materials. The possibility of increasing vacancy concentrations by substitutional doping (F for O in Li_3BO_3 and C for B in Li_3BN_2) is also examined, finding simulated conductivities comparable to those of the ideal vacancy model.

DOI: 10.1103/PhysRevMaterials.5.085402

I. INTRODUCTION

There has been considerable progress in developing inorganic Li ion conducting solid electrolytes for a variety of technologies such as all-solid-state lithium ion batteries for energy storage and delivery and for thin film sensors, as evidenced in a number of recent reviews [1–8]. Some of the current challenges for materials science include optimizing the ion conductivity and stability of solid electrolytes and stabilizing the interfaces between solid electrolytes and electrodes, particularly working toward stabilizing metallic Li as a very efficient anode. For example, nitride and oxide electrolytes such as lithium oxynitride (LIPON) are known [9–12] to show excellent stability with Li metal anodes and cathodes. Rather than developing a single material that meets all of the technological requirements, one promising approach has been to develop composite materials and coatings such as described by Richards *et al.* [13]. In the search for further optimization, boron-based materials have been gaining considerable interest because of their general availability, nontoxicity, and demonstrated success in related technologies such as high-strength borosilicate glass. Additionally, from a technical viewpoint, it is known that boron-based materials are likely to be adaptable to efficient processing techniques such as atomic layer deposition, sol-gel-based processes, and spray coating procedures. In this paper and in the companion paper (Paper II [14]), we examine two boron-based materials which have been identified as good Li ion conductors—Li_3BO_3 and Li_3BN_2—with possible applications as Li ion electrolytes or coatings.

The literature reports promising electrolyte properties of Li_3BO_3 and Li_3BN_2. Ohta *et al.* [15] reported the use of Li_3BO_3 as an intermediate electrolyte to stabilize the interface between a $LiCoO_2$ cathode and a lithium garnet oxide electrolyte in an all-solid-state battery. Li_3BO_3 was found to provide a structurally stable contact between the cathode and the garnet electrolyte. In the context of solid electrolytes, the experimental studies [16–23] show Li_3BO_3-based glass and glass-ceramic solid electrolytes exhibit relatively high ionic conductivities in the range of $10^{-7} - 10^{-5}$ S/cm at room temperature. Li_3BN_2 is a ternary compound similar to Li_3BO_3. In addition to its electrolyte properties, several other applications have been explored. For example, the material was explored as a promising material for hydrogen storage applications [24,25] and it was also studied as solvent catalyst for synthesizing the cubic BN from hexagonal BN [26–28]. There has also been some work exploring α-Li_3BN_2 as a cathode material for Li ion batteries [29]. The present paper focuses on the performance of Li_3BN_2 as a potential solid electrolyte or coating material. In the 1987 paper by Yamane *et al.* [30], two crystalline phases of Li_3BN_2 were prepared from Li_3N and BN binary compounds. The measured ionic conductivity for a polycrystalline sample at 400 K was reported to be 3×10^{-7} S/cm. Shigeno *et al.* [31] recently showed that a "glass-ceramic" form of Li_3BN_2, with a similar x-ray pattern to monoclinic β-Li_3BN_2, has a room temperature conductivity of 1.1×10^{-7} S/cm, several orders of magnitude higher than the room-temperature conductivity of crystalline α-Li_3BN_2.

Li_3BO_3 and Li_3BN_2 share some common features. For both, the relatively high conducting phase has a monoclinic $P2_1/c$ (space group No. 14) [32,33] structure (α form for Li_3BO_3 and β form for Li_3BN_2). However, to the best of our knowledge, the detailed mechanisms of the Li-ion diffusion in these materials has not yet been reported in the literature.

A comprehensive computational study of Li_3BO_3 and Li_3BN_2 is presented in two papers. This paper (Paper I) focuses on analyzing Li ion mobilities, important for electrolyte functionality, and is organized as follows. Section II presents the computation methods used in this paper. The models of pure and doped materials for Li ion migration are discussed in Sec. III. Sections IV and V analyze Li ion diffusion mechanisms using the nudged elastic band (NEB) method [34–36] and molecular dynamics (MD) simulations, respectively. Exploring possibilities for optimizing ionic conductivity, vacancy, and interstitial mechanisms in the bulk pure and doped models of Li_3BO_3 and Li_3BN_2, are investigated. A summary and conclusions of this paper are given in Sec. VI. Paper II [14] analyzes the structural and chemical stabilities of bulk Li_3BO_3 and Li_3BN_2 and their interfaces with ideal metallic Li.

II. CALCULATIONAL METHODS

The computational methods for this paper are based on density functional theory [37,38] using the projector augmented plane wave [39] formalism with the data sets generated by the ATOMPAW code [40]. All calculations in this paper were performed using the QUANTUM ESPRESSO [41,42] package with the modified generalized gradient formulation known as PBEsol [43] to describe the exchange-correlation effects. In this paper, all simulations are based on the monoclinic structures optimized as described in Paper II [14]. For this paper, focusing on transport, convergence parameters could be slightly less stringent compared with those used in Paper II. Here we used the plane wave expansion cutoff $2m|\mathbf{k}+\mathbf{G}|^2/\hbar^2 \leqslant 64$ Ry. Interestingly, while the two materials have the same space group, their dimensions are quite different. For simulating Li ion diffusion in Li_3BO_3, simulations were performed using a $3 \times 1 \times 1$ supercell of the conventional cell having 84 atoms and approximately equal lattice lengths (9.73, 9.17, and 8.24 Å) for the a, b, and c directions, respectively. The ionic transport properties investigated for β-Li_3BN_2 are based on a $2 \times 2 \times 1$ supercell containing 96 atoms with similar lattice lengths (10.22, 14.00, and 6.71 Å) for the a, b, and c directions, respectively. For the MD and NEB simulations in these relatively large supercells, the k-point sampling could be reduced from that described in Paper II which focused on detailed energetics and structures. Here, the k-point sampling could be reduced to a few or even a single sampling point as evidenced by convergence studies on representative NEB calculations.

The structural configurations were visualized using the VESTA [44] and XCRYSDEN [45] programs.

III. MODELS FOR LI ION MIGRATION

As discussed in Paper II [14], both Li_3BO_3 and Li_3BN_2 in their $P2_1/c$ monoclinic (space group No. 14) [32,33] structures are well-ordered. They both are densely packed with limited space available for Li ion motion. Analysis of Li ion migration necessarily involves identifying metastable defects including interstitials and vacancies.

To estimate the metastable interstitial positions in the ideal crystals, we searched for the lowest energy optimized structures of supercells of the ideal crystals augmented with an additional Li ion (and with a uniform distribution of compensating charge). In this study, we found one such ideal interstitial I-int site for each material based on a $3 \times 1 \times 1$ supercell for Li_3BO_3 and a $2 \times 2 \times 1$ supercell for Li_3BN_2. These I-int sites are also useful for estimating the energy to form a vacancy-interstitial pair defect, E_f, from the energy difference of the lowest nontrivial energy for an optimized vacancy-interstitial structure relative to its corresponding perfect supercell.

In this paper, we considered two types of vacancy defects. An ideal vacancy defect I-vac was modeled using optimized structures of supercells of the ideal crystals diminished with a missing Li ion (and with a uniform distribution of compensating charge). We also considered various ion substitutions in the supercell to model a neutral Li ion vacancy material. These are referenced as a F-doped vacancy for Li_3BO_3 and as a C-doped vacancy for Li_3BN_2. The choice of F substituting for O in Li_3BO_3 and C substituting for B in Li_3BN_2 represent exploratory design possibilities for increasing ionic conductivity following similar strategies described in the literature [46–48], including other possibilities for these materials [21,49,50].

To estimate defect-induced atomic distortions relative to the perfect crystal structure, we followed the approach of Lepley and Holzwarth [51] to calculate the averaged atomic distortion parameter,

$$\bar{D}^a = \frac{1}{N^a} \sum_{i=1,\in N^a}^{N^a} \left|\Delta \mathbf{R}_i^a\right|, \tag{1}$$

and the maximum distortion parameter,

$$D^a_{\max} = \max_{i \in N^a} \left|\Delta \mathbf{R}_i^a\right|. \tag{2}$$

In these equations, N^a denotes the number of ions of type a and $\Delta \mathbf{R}_i^a$ denotes the difference in the position of the ith ion of type a in the optimized structure of the defective lattice relative to its position in the ideal lattice. For the case of vacancy defects, the vacancy site is omitted from the analysis in Eqs. (1) and (2). For the F-doped and C-doped models, we allowed only one substitutional site in the supercell so the corresponding $N^a = 1$ and the average and maximum distortion measures are equal: $D^a = D^a_{\max}$.

A. Defect models for Li_3BO_3

The lowest energy metastable interstitial sites are visualized with green balls in Fig. 1 in the $3 \times 1 \times 1$ supercell. Referenced to the unit cell of the $P2_1/c$ structure, these I-int sites map closely to the multiplicity and Wyckoff label $2b$ with example fractional coordinates (0.5, 0.5, 0.5). The corresponding vacancy-interstitial pair formation energy is estimated to be $E_f = 1.25$ eV. Because of this high formation energy and relatively large distance between I-int sites within the crystal structure (>3.24 Å), we expect that interstitial mechanisms play a minimal role in Li ion migration for Li_3BO_3.

There are three inequivalent Li ion sites in Li_3BO_3 and correspondingly three distinct I-vac energies. The site labels in Fig. 1 indicate a possible Li ion vacancy migration path in the $3 \times 1 \times 1$ supercell in terms of an I-vac site moving

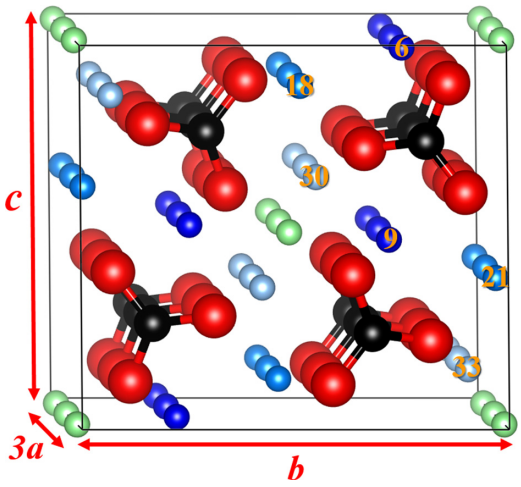

FIG. 1. Ball and stick diagram of Li_3BO_3 with Li, B, and O represented by three shades of blue, black, and red balls, respectively. Dark, medium, and light blue shades correspond to Li(1), Li(2), and Li(3) types, respectively. Equivalent I-int sites are shown with green balls.

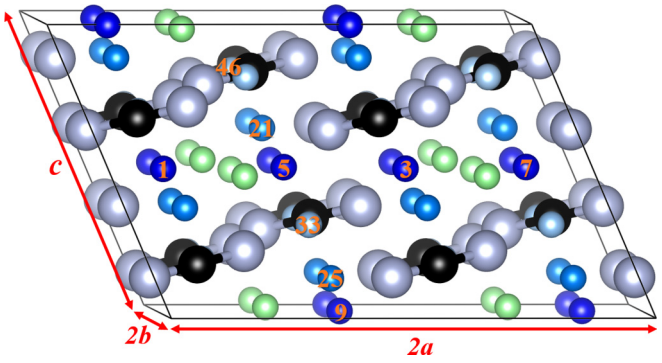

FIG. 2. Ball and stick diagram of Li_3BO_3 with Li, B, and N represented by three shades of blue, black, and gray balls, respectively. Dark, medium, and light blue shades correspond to Li(1), Li(2), and Li(3) types, respectively. Equivalent I-int sites are shown with green balls.

successively according to the labels $6 \rightarrow 18 \rightarrow 30 \rightarrow 9 \rightarrow 21 \rightarrow 33 \rightarrow 6$. In this case, the geometrically equivalent sites are $9 \equiv 6$, $21 \equiv 18$, and $33 \equiv 30$. These correspond to the Li(1)-, Li(2)-, and Li(3)-type labels discussed in Paper II [14], respectively. From the optimized structures of the geometrically distinct Li sites, we find that the I-vac energies are very similar. It is convenient to set the I-vac energy of site $18 \equiv 21$ to be zero. The results, together with the distortion measures, are summarized in Table I, given below. The table shows that for these I-vac defects, the largest average distortion is 0.07 Å or less and the Li host lattice sites experience the largest maximum distortions of 0.43 Å or less.

Because of the large vacancy-interstitial pair formation energy E_f, it is advantageous to consider electrolytes formed from Li_3BO_3 materials modified to have a native concentration Li ion vacancies. One way to accomplish this is to substitute x O ions with x F ions while removing x Li ions forming $Li_{3-x}BO_{3-x}F_x$. For the $3 \times 1 \times 1$ supercell, $x = 1/12$ and Table I also reports the results for optimized structures this model system, compared with the corresponding I-vac models. For the F-doped models, the Li vacancy energies are no longer equal, with the vacancy configuration on the site closest to the substitutional F site (in this case, site 33) having the lowest energy and set to 0. For the F-doped models [illustrated in Fig. 3(a) below], the distortion measures are all larger than for the I-vac models, with the largest increases for the Li sites.

To estimate the stability of F-doped Li_3BO_3, we considered the following possible decomposition reaction:

$$Li_{3-x}BO_{3-x}F_x \rightarrow (1-2x)Li_3BO_3 + 2xLi_2O + xB_2O_3 + xLiF, \quad (3)$$

where $x = 1/12$ in this simulation. For simplicity, the reaction energy ΔU_{SL}, estimated on the basis of the static lattice energies only, was calculated from the energy of $Li_{3-x}BO_{3-x}F_x$ minus the energy of the products on the right-hand side of Eq. (3). The product LiF has a cubic structure with space group $Fm\bar{3}m$ (No. 225) and the information for the rest of the products can be found in Paper II. The minimum value of the six vacancy configurations considered (for the vacancy on site 33) was found to be $\Delta U_{SL} = -0.06$ eV. This negative value suggests that F-doped Li_3BO_3 is stable at least with respect to the modeled decomposition.

B. Defect models for Li_3BN_2

While Li_3BN_2 (in its β phase) has the same space group as Li_3BO_3, the atomic arrangement is quite distinct, as discussed

TABLE I. The relative vacancy energies in eV and distortion parameters (in Å) as calculated according to Eqs. (1) and (2) for the I-vac and F-doped Li_3BO_3. The labels in the first column refer to the vacancies displayed in Fig. 1, the column dis (in Å) gives the distance between the F substitutional site and the corresponding Li vacancy, measured from the host sites in the perfect crystal before relaxation.

	I-vac				F-doped				
Label	E_v	$\bar{D}^{Li}/D^{Li}_{max}$	$\bar{D}^{B}/D^{B}_{max}$	$\bar{D}^{O}/D^{O}_{max}$	E_v/dis	$\bar{D}^{Li}/D^{Li}_{max}$	$\bar{D}^{B}/D^{B}_{max}$	$\bar{D}^{O}/D^{O}_{max}$	$\bar{D}^{F}/D^{F}_{max}$
No. 6	0.04	0.05/0.29	0.03/0.09	0.05/0.21	0.30/3.93	0.11/0.83	0.06/0.14	0.07/0.24	0.15/0.15
No. 18	0.00	0.07/0.43	0.04/0.14	0.05/0.19	0.24/4.71	0.12/1.02	0.06/0.13	0.07/0.22	0.09/0.09
No. 30	0.02	0.07/0.34	0.04/0.13	0.06/0.24	0.40/5.60	0.10/0.35	0.06/0.17	0.07/0.25	0.08/0.08
No. 9	0.04	0.05/0.29	0.03/0.09	0.05/0.21	0.41/4.93	0.09/0.35	0.05/0.15	0.06/0.21	0.05/0.05
No. 21	0.00	0.07/0.43	0.04/0.14	0.05/0.19	0.23/3.30	0.10/0.41	0.06/0.17	0.07/0.18	0.07/0.07
No. 33	0.02	0.07/0.34	0.04/0.13	0.06/0.24	0.00/1.96	0.08/0.34	0.05/0.13	0.06/0.23	0.14/0.14

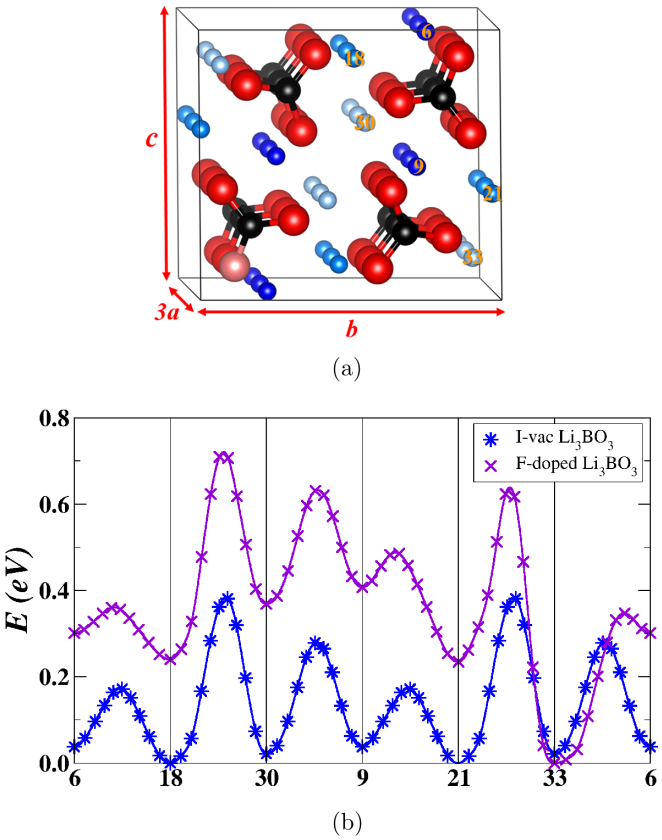

FIG. 3. (a) Ball and stick diagram for vacancy migration in Li_3BO_3 with Li, B, O, and F represented by three shades of blue, black, red, and pink balls, respectively. Labels indicate vacancy sites for migration pathway. (b) Configuration energy diagram results of NEB calculation of Li ion vacancy migration along the indicated pathway. The energies for these diagrams are adjusted for the lowest energy of the considered configurations, consistent with Table I.

in Paper II [14]. The lowest energy metastable interstitial sites are visualized with green balls in Fig. 2 in the $2 \times 2 \times 1$ supercell. Referenced to the unit cell of the $P2_1/c$ structure, these I-int sites map closely to the multiplicity and Wyckoff label 4*e* with example fractional coordinates (0.560, 0.279, 0.978). The corresponding vacancy-interstitial pair formation energy is estimated to be $E_f = 1.23$ eV. Although this is a relatively high formation energy, because of the relatively small distances between I-int sites within the crystal structure (2.91 Å), we expect that interstitial mechanisms may play a role in Li ion migration for Li_3BN_2.

There are three inequivalent Li ion host sites in Li_3BN_2 and correspondingly three distinct I-vac energies. The site labels in Fig. 2 indicate two possible Li ion vacancy migration paths in the $2 \times 2 \times 1$ supercell which will be considered in Sec. IV B below. From the optimized structures of the geometrically distinct Li sites, we find that the I-vac energies for sites Li(1) and Li(2) are very similar, while I-vac energy for site Li(3) (light blue balls in Fig. 2) are 0.51 eV higher, which might be attributed to its strong Coulomb interactions with neighboring $(BN_2)^{-3}$ ions. It is convenient to set the I-vac energy of site $21 \equiv 25$ to be zero. The results together with the distortion measures are summarized in Table II given below. The table shows that for these I-vac defects, the largest average distortion is 0.07 Å or less and the Li host lattice sites experience the largest maximum distortions of 0.62 Å or less.

As for Li_3BO_3, it is reasonable to expect that it is advantageous to consider electrolytes formed from Li_3BN_2 materials modified to have native concentration Li ion vacancies. One way to accomplish this is to substitute x B ions with x C ions and to remove x Li ions, forming $Li_{3-x}B_{1-x}C_xN_2$. For the $2 \times 2 \times 1$ supercell, $x = 1/16$ and Table II also reports the results for the optimized structures of this model system, compared with the corresponding I-vac models. For the C-doped models, the Li vacancy energies are no longer equal, with the vacancy configuration having the lowest energy (site 25) set to 0. For the C-doped models [illustrated in Fig. 4(a) below], the distortion measures for the Li sites are all larger than those for the I-vac models.

Analogous to the case of the F-doped Li_3BO_3, the replacement of B with C breaks the symmetry of the original structure of the Li_3BN_2, resulting in multiply inequivalent Li vacancies with the lowest metastable energy occurring for the vacancy configuration at site 25, which is 3.19 Å away from the position of the C dopant. As indicated in Table II, the C dopant

TABLE II. The relative vacancy energies in eV and distortion parameters (in Å) as calculated according to Eqs. (1) and (2) for the I-vac and C-doped Li_3BN_2. The labels in the first column refer to the vacancies displayed in Fig. 2, the column dis (in Å) gives the distance between the C substitutional site and the corresponding Li vacancy, measured from the host sites in the perfect crystal before relaxation.

	I-vac				C-doped				
Label	E_v	$\bar{D}^{Li}/D^{Li}_{max}$	$\bar{D}^{B}/D^{B}_{max}$	$\bar{D}^{N}/D^{N}_{max}$	E_v/dis	$\bar{D}^{Li}/D^{Li}_{max}$	$\bar{D}^{B}/D^{B}_{max}$	$\bar{D}^{C}/D^{C}_{max}$	$\bar{D}^{N}/D^{N}_{max}$
No. 1	0.03	0.07/0.62	0.03/0.09	0.06/0.22	0.11/2.38	0.07/0.46	0.40/0.11	0.02/0.02	0.07/0.20
No. 5	0.03	0.07/0.62	0.03/0.09	0.06/0.22	0.06/3.10	0.07/0.35	0.03/0.09	0.11/0.11	0.06/0.23
No. 3	0.03	0.07/0.62	0.03/0.09	0.06/0.22	0.28/5.00	0.08/0.57	0.04/0.08	0.05/0.05	0.07/0.23
No. 7	0.03	0.07/0.62	0.03/0.09	0.06/0.22	0.17/4.05	0.08/0.58	0.04/0.09	0.04/0.04	0.07/0.23
No. 46	0.51	0.06/0.40	0.04/0.08	0.06/0.18	0.91/7.92	0.09/0.39	0.05/0.10	0.02/0.02	0.08/0.39
No. 21	0.00	0.06/0.35	0.04/0.10	0.07/0.27	0.33/5.66	0.08/0.42	0.05/0.09	0.03/0.03	0.09/0.28
No. 33	0.51	0.06/0.40	0.04/0.08	0.06/0.18	0.56/2.60	0.07/0.43	0.04/0.10	0.06/0.06	0.06/0.23
No. 25	0.00	0.06/0.35	0.04/0.10	0.07/0.27	0.00/3.19	0.07/0.27	0.03/0.05	0.11/0.11	0.07/0.25
No. 9	0.03	0.07/0.62	0.03/0.09	0.06/0.22	0.38/5.72	0.10/0.65	0.04/0.10	0.02/0.02	0.08/0.23

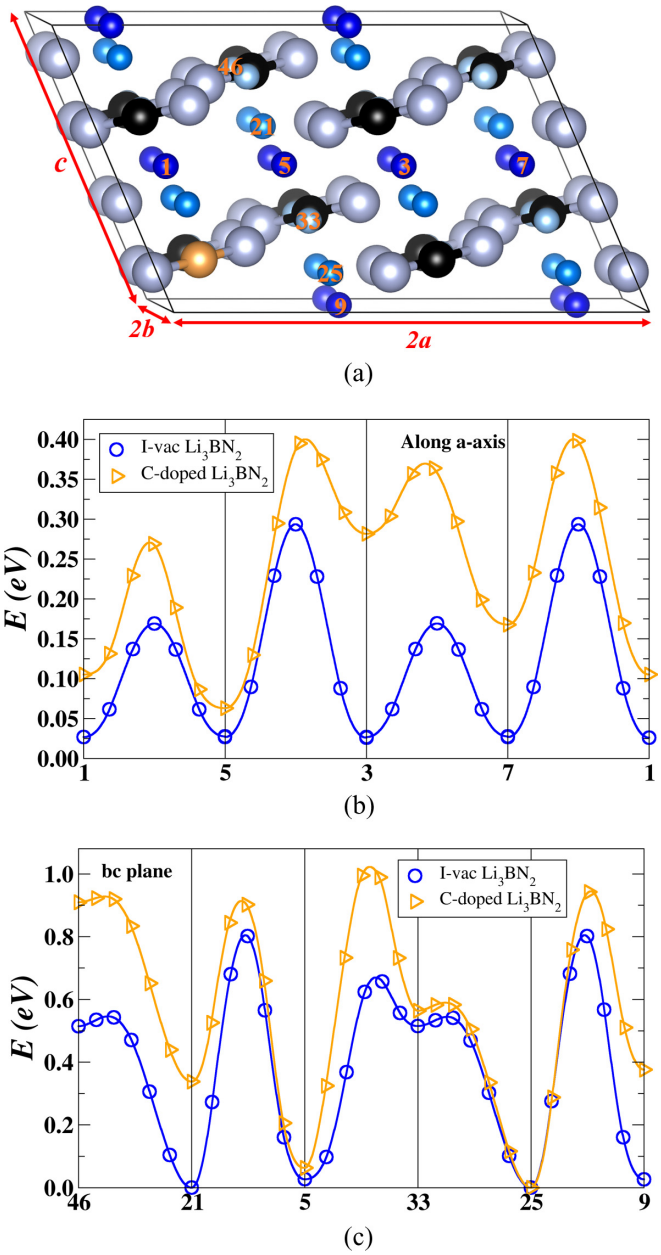

FIG. 4. (a) Ball and stick diagram for vacancy migration in Li_3BN_2 with Li, B, C, and N ions represented by three shades of blue, black, brown, and gray balls, respectively. Labels indicate vacancy sites for migration pathways. The configuration energy diagrams from NEB calculations for Li ion vacancy migrations along the **a** axis and within **bc** plane are shown in (b) and (c), respectively. The energies for these diagrams are adjusted for the lowest energy of the considered configurations, different for the I-vac and C-doped models and consistent with Table II.

tends to reduce the energy of the defect structure in which the vacancy is close to it, and at the same time undergoes greater deformation during optimization. However, it is evident that the vacancy energy pattern for the C-doped model is affected by more than proximity to the C site. For example, site 1 is closest to the C site with a distance of 2.38 Å but has an energy of 0.11 eV while the vacancy at site 33 is 2.60 Å away from the C site but its energy is up to 0.56 eV.

To estimate the stability of C-doped Li_3BN_2, we considered the following possible decomposition reaction:

$$Li_{3-x}B_{1-x}C_xN_2 \rightarrow (1-x)Li_3BN_2 + xLi_2CN_2, \quad (4)$$

where $x = 1/16$ in this simulation. For simplicity, the reaction energy ΔU_{SL} was estimated from the static lattice contributions of $Li_{3-x}B_{3-x}C_xN_2$ minus the energy of the productions on the right-hand side of Eq. (4). The structure for the product Li_2CN_2 has space group symmetry $I4/mmm$ (No. 139) and was optimized based on the experimental data reported in Ref. [52]. The minimum value of the nine vacancy configurations considered (for the vacancy on site 25) was found to be $\Delta U_{SL} = +0.05$ eV. This positive value suggests that C-doped Li_3BN_2 may need special treatment to actually synthesize. However, since the doped structure is computationally stable, we include the simulation results for reference. In practice, it is known that Li_3BN_2 samples are sensitive to surface oxygen degradation.

IV. LI ION MIGRATION ANALYSIS VIA THE ELASTIC BAND METHOD

The NEB method [34–36] has been well developed to evaluate the temperature (T) dependence ion diffusion coefficient $D(T)$ according to the Arrhenius form

$$D(T) = D_0 e^{-E_a^{NEB}/k_B T}, \quad (5)$$

where k_B denotes the Boltzmann constant and D_0 is the temperature-independent pre-exponential factor. For the NEB analysis, the ion migration energy barrier E_m^{NEB} for a predefined migration path is determined from the highest energy found along the constructed NEB path relative to a reference defect energy of the supercell. The relationship of the activation energy E_a^{NEB} to E_m^{NEB} depends on the system under consideration. In general, we expect that the activation energy varies in a range:

$$\epsilon_{min} \leqslant E_a^{NEB} \leqslant \epsilon_{max}. \quad (6)$$

In this paper, we consider two types of systems—defective and ideal materials. Substitutionally doped materials, or materials prepared with poor crystallinity, are expected to have a substantial population of defects, so the activation energy for ionic diffusion is expected to be close to the minimum:

$$\epsilon_{min} = E_m^{NEB} = \max(\Delta E_m + E_d^0). \quad (7)$$

Here, ΔE_m denotes the energy barrier calculated from the NEB formalism for a single hop step and E_d^0 represents the lowest defect energy such as listed in Tables I and II for the particular migration path. The E_d^0 contribution comes from the expectation that there is a temperature-dependent probability associated with the particular path, determined by the equilibrium population of the lowest energy defect sites as determined by a Boltzmann distribution [53]. For more ideal samples not having a population of vacancies or interstitials, it is assumed that the migration process is initiated by moving one Li ion at a host lattice site into an interstitial site, the activation energy for ionic conductivity E_a^{NEB} therefore additionally includes the defect formation energy E_f which is associated with a formation of vacancy-interstitial pair with

TABLE III. Vacancy hopping energies ΔE_m for Li_3BO_3 for the I-vac and F-doped models. The step labels refer to the position labels in Fig. 3(a). The distances (measured from the perfect crystal sites before defect optimization) are given in units of Å and energies are given in eV units.

		ΔE_m	
Step	Distance	I-vac	F-doped
6 ↔ 18	2.51	0.17	0.12
18 ↔ 30	2.69	0.38	0.48
30 ↔ 9	2.48	0.26	0.26
9 ↔ 21	2.51	0.17	0.25
21 ↔ 33	2.69	0.38	0.64
33 ↔ 6	2.48	0.26	0.35

the maximum value [54]:

$$\epsilon_{\max} = E_m^{\mathrm{NEB}} + \tfrac{1}{2}E_f = \max\left(\Delta E_m + E_d^0\right) + \tfrac{1}{2}E_f. \quad (8)$$

A. NEB analysis for Li_3BO_3

As illustrated in Fig. 3, we identified the main diffusion path to be composed of sites 6 ↔ 18 ↔ 30 ↔ 9 ↔ 21 ↔ 33 ↔ 6 in both the I-vac and the F-doped Li_3BO_3. The labels and energies correspond to the vacancy energies and distortion parameters listed in Table I. While this path is not the only possibility, it illustrates an efficient migration pathway within the **bc** plane.

The configuration path diagram shows that for the I-vac model, we see that the highest barrier for Li vacancy migration occurs between sites 18 and 30 or equivalently between sites 21 and 33 involving type Li(1) and Li(2) sites. By contrast, the F-doped model shows that the substitutional F ion tends to trap a Li ion vacancy in its vicinity (site 33 in this case). However, vacancy sites further away from the substitutional F site appear to resemble the I-vac energy path, shifted by approximately 0.2 eV. It is presumed that the simulations in larger supercells would converge more accurately to the I-vac energy profile.

The quantitative comparison between vacancy diffusion in Li_3BO_3 is summarized in Table III. For the I-vac crystal, the diffusion path consists of two symmetrically equivalent paths 6 ↔ 18 ↔ 30 ↔ 9 and 9 ↔ 21 ↔ 33 ↔ 6, resulting in two periodically repeated energy profiles with maximum step barrier of $\Delta E_m = 0.38$ eV occurring for 18 ↔ 30 and 21 ↔ 33. The energy barrier of each path segment in the F-doped crystal is comparable to that of the I-vac crystal. However, the hop between sites 21 ↔ 33 requires a higher energy of $\Delta E_m = 0.64$ eV compared to $\Delta E_m = 0.38$ eV in the I-vac structure, suggesting the F dopant tends to trap the vacancy close to the doping site. For path 30 ↔ 9 which is furthest from the F site, the doping effect is negligible with the same hopping energy of $\Delta E_m = 0.26$ eV as for the I-vac structure. From this analysis, we can estimate the activation energies for Li ion migration. According to Eq. (7), we find that $E_m^{\mathrm{NEB}} = 0.38$ eV for the ideal I-vac model, compared with $E_m^{\mathrm{NEB}} = E_a^{\mathrm{NEB}} = 0.72$ eV for the F-doped model. For a stoichiometric and well-crystallized sample without presence of any defects, the vacancy-interstitial pair formation energy E_f energy enters according to Eq. (7), resulting in the estimate $E_a^{\mathrm{NEB}} = 1.00$ eV. While the F-doped model tends to trap the Li ion vacancy near the doping site, the estimate of the activation for Li ion migration energy is lower than that of the perfect crystal. As a consequence, doping with substitutional F provides an encouraging approach to improve the ionic conductivity properties of the pure Li_3BO_3 crystal. Alternatively, a stoichiometric but poorly crystalline sample would be expected to be represented by the I-vac model with an activation energy of $E_m^{\mathrm{NEB}} = E_a^{\mathrm{NEB}} = 0.38$ eV.

B. NEB analysis for Li_3BN_2

Among several possible migration paths of I-vac and C-doped models of Li_3BN_2 crystals, we present two representative Li ion vacancy migrations along the **a** axis and within a **bc** plane as illustrated in Fig. 4, with corresponding vacancy energies and distortion parameters listed in Table II. It is worth mentioning that the zero of energy was taken separately for the I-vac and C-doped models. The pure Li_3BN_2 contains three inequivalent Li sites: Li(1), Li(2), and Li(3) as indicated by three shades of blue balls in Fig. 4(a), consequently there are three distinct metastable vacancy configurations. For this I-vac case, the migration energy of each NEB channel was referenced to the energy of configuration with Li(2)-type vacancy at site 21 and its equivalent 25. For the C-doped model, site 25 has the lowest energy of the configurations considered and is set to zero energy, while sites further from the substitutional C site start to resemble the I-vac profile shifted to higher energy by approximately 0.3 eV.

The NEB energy diagrams for the I-vac and C-doped structures are shown in Fig. 4(b) for a path involving Li(1) vacancies sites moving along the **a** axis and Fig. 4(c) for a path involving alternating Li(1), Li(2), and Li(3) vacancy sites within in a **bc** plane. The quantitative analysis of vacancy diffusion in Li_3BN_2 is summarized in terms of the hopping energy barrier ΔE_m in Table IV based on the highest barrier for each indicated step. Since the supercell of the I-vac model of Li_3BN_2 consists of two replicas of the conventional unit cell along the **a** axis, the four-step path 1 ↔ 5 ↔ 3 ↔ 7 ↔ 1 involves two periodic energy profiles between nearest-neighbor sites of the same Li(1)-type: 1 ↔ 5 ↔ 3 and 3 ↔ 7 ↔ 1. Dominated by the migration path between 5 ↔ 3 (7 ↔ 1), the maximum energy barrier that a Li ion has to overcome for consecutive hops along this one-dimensional channel is $\Delta E_m = 0.27$ eV, together with the minimum defect energy $E_d^0 = 0.03$ eV, it can determine the migration energy of $E_m^{\mathrm{NEB}} = 0.30$ eV for this path of the I-vac model from Eq. (7). Taking into account the estimated vacancy-interstitial pair formation energy of $E_f = 1.23$ eV, the activation energy for the perfect crystal is calculated to be $E_a^{\mathrm{NEB}} = 0.62$ eV according to Eq. (8). Generally, the migration barrier for Li ion diffusion in the C-doped Li_3BN_2 not only depends on the position of the C dopant but also depends on the surrounding environment experienced by the mobile Li ions. For example, for the C-doped model, the corresponding **a** axis vacancy migration path finds the controlling barrier for the overall process to be the step 5 ↔ 3 with $\Delta E_m = 0.34$ eV, which together with the reference defect energy of $E_d^0 = 0.06$ eV, estimates $E_a^{\mathrm{NEB}} = E_m^{\mathrm{NEB}} = 0.40$ eV according to Eq. (7).

TABLE IV. Defect hopping energies ΔE_m for I-vac, C-doped, and I-int models of Li_3BN_2. The step labels refer to the position labels in Fig. 4(a) for I-vac and C-doped models or the inset figure in Fig. 5 for the I-int models. The distances (measured from the corresponding perfect crystal sites before defect optimization) are given in units of Å and energies are given in eV units.

			ΔE_m	
Mechanism	Step	Distance	I-vac	C-doped
Vacancy along **a** axis	$1 \rightarrow 5$	2.57	0.14	0.21
	$5 \rightarrow 3$	2.57	0.27	0.34
	$3 \rightarrow 7$	2.57	0.14	0.20
	$7 \rightarrow 1$	2.57	0.27	0.30
Vacancy in **bc** plane	$46 \rightarrow 21$	2.49	0.55	0.59
	$21 \rightarrow 5$	3.38	0.81	0.85
	$5 \rightarrow 33$	2.51	0.64	0.96
	$33 \rightarrow 25$	2.49	0.55	0.59
	$25 \rightarrow 9$	3.38	0.81	0.95
Kick out	$I3 \rightarrow 1 \rightarrow I1$	–	0.52	–
	$I1 \rightarrow 21 \rightarrow I4$	–	0.30	–
	$I4 \rightarrow 2 \rightarrow I2$	–	0.52	–

The Li ion diffusion in the **bc** plane of the I-vac and C-doped models of Li_3BN_2 involves a series of zigzag steps between adjacent inequivalent vacancy sites $46 \leftrightarrow 21 \leftrightarrow 5 \leftrightarrow 33 \leftrightarrow 25 \leftrightarrow 9$. The barriers for each step are summarized in Table IV. For the I-vac model of Li_3BN_2, the path $46 \leftrightarrow 21 \leftrightarrow 5$ is symmetrically equivalent to the path $33 \leftrightarrow 29 \leftrightarrow 9$ with a hopping energy of $\Delta E_m = 0.81$ eV. This suggests that for a poorly crystalline sample of stoichiometric Li_3BN_2, the activation energy would be $E_a^{\mathrm{NEB}} = E_m^{\mathrm{NEB}} = 0.81$ eV while for a well-crystallized sample the activation energy would be $E_a^{\mathrm{NEB}} = 1.43$ eV, according to Eqs. (7) and (8), respectively. The corresponding hopping energies for the C-doped model are comparable, but because of the greater stability of the vacancy at site 46 near the C substitutional site, the largest hopping barrier is found to be $\Delta E_m = 0.96$ eV for the $5 \leftrightarrow 33$ step. The activation energies for this path in the **bc** plane is computed from Eq. (7) to be $E_a^{\mathrm{NEB}} = 1.02$ eV. Generally, the Li ion migration barriers in the **bc** plane are significantly larger than those in along the **a** axis.

Also listed in Table IV are results from NEB analyses involving the equivalent lowest energy metastable interstitial sites. Figure 5 shows the corresponding local ball and stick diagram containing four equivalent nearest-neighboring interstitial sites I1–I4 surrounded by Li ions at host sites of types Li(1) and Li(2) together with the corresponding energy path diagram. Although direct hopping between interstitial sites seems to be unlikely on the basis of geometric considerations, kick-out or interstitiacy processes may be possible. This was examined using the results from the I-int models discussed in Sec. III B to model $2 \times 2 \times 1$ supercells of Li_3BN_2 containing one charge-compensated interstitial Li ion. The corresponding hopping energies ΔE_m are listed at the bottom of Table IV. Here the notation $I3 \rightarrow 1 \rightarrow I1$ means that an initial I-int configuration at the interstitial site I3 (visualized in the insert of Fig. 5) transitions to replace the host Li ion at site 1, which then moves to I-int configuration at the interstitial site I1. The

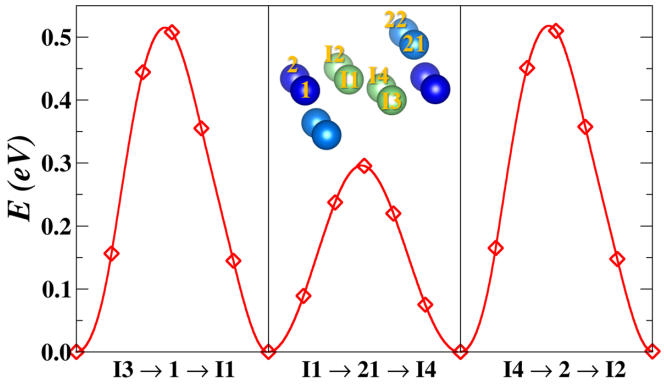

FIG. 5. Configuration energy diagram for the kick-out mechanism in Li_3BN_2 together with an inset diagram of the involved sites. In the diagram, Li ions at host sites are represented using the same convention as in Fig. 4(a) while interstitial sites are represented with green balls.

subsequent step of $I1 \rightarrow 21 \rightarrow I4$ is geometrically equivalent to the initial configuration in this supercell. Proceeding with this kick-out process, Li ions can consecutively hop between equivalent interstitial sites with the exchange of host ions between type-Li (1) and -Li (2) sites, resulting in a net motion along the **b** axis. The maximum hopping energy for the path $I3 \rightarrow 1 \rightarrow I1 \rightarrow 21 \rightarrow I4$ is $\Delta E_m = 0.52$ eV. According to Eqs. (7) and (8), the activation energy for this process is expected to be $E_a^{\mathrm{NEB}} = 0.52$ or 1.14 eV for a poorly crystalline or highly crystalline sample, respectively.

In summary, the NEB analysis suggests that the most efficient Li ion conductivity in Li_3BN_2 occurs via a vacancy mechanism along the a axis of the crystal.

V. MOLECULAR DYNAMICS SIMULATIONS

MD simulations based on density-functional evaluations of the ideal and defective supercells were performed to understand the dynamic and statistical nature of Li ion migrations. The simulations approximated a microcanonical NVE ensemble, using a velocity Verlet algorithm [55] with a time integration step of $\Delta t = 2.4$ fs. Here NVE refers to a constant number of atoms N_{atom} in the supercell held at constant volume V and a constant energy which corresponds to $U_{\mathrm{SL}} + E_{\mathrm{kin}}^{\mathrm{ion}}$, the total density functional static lattice energy plus the classical mechanics ion kinetic energy at each time step. The initial distribution of velocities of ions in the relaxed simulation cell is taken from Boltzmann distribution for twice the target temperature. Without controlling the temperature via any velocity rescaling scheme, this procedure is found to equilibrate for simulations times $t > t_{\mathrm{eq}}$, with fluctuating instantaneous temperatures around the target temperature. For most of the simulations in this paper, $t_{\mathrm{eq}} \approx 0.02$ ps. Typically, the average temperature for a given run is determined by averaging the temperature from the ion classical kinetic energy at each time step t' according to

$$\langle T \rangle = \frac{2}{3(N_{\mathrm{atom}} - 1)k_B} \frac{1}{(t_{\mathrm{max}} - t_{\mathrm{eq}})} \int_{t_{\mathrm{eq}}}^{t_{\mathrm{max}}} E_{\mathrm{kin}}^{\mathrm{ion}}(t')dt'. \quad (9)$$

In this paper, a sufficiently high temperature is required to simulate significant hopping events in the model structures. We find that although $\langle T \rangle$ is generally close to the target temperature, it is somewhat dependent on the setting of the initial velocity distribution. The ionic conductivity for each system under consideration is obtained after a MD duration of 100–120 ps.

In this paper, the ionic motion is analyzed with the simplifying assumption that independent ion motion dominates, focusing on the so-called tracer diffusion process which depends on the mean-squared displacement (MSD) [56,57]. With equally probable microscopic states at each time step, the MSD, defined by the following relation, is introduced to track the dynamical evolution of Li ions over a time window of t for a simulated temperature T:

$$\mathrm{MSD}(t, T) \equiv \frac{1}{N_{\mathrm{Li}}} \left\langle \sum_{i=1}^{N_{\mathrm{Li}}} |\mathbf{R}_i(t) - \mathbf{R}_i(0)|^2 \right\rangle_t, \tag{10}$$

where N_{Li} indicates the number of mobile Li ions in the simulation and $\mathbf{R}_i(t)$ denotes the position of the Li ion with label i at time t. During the simulations over the total time duration, there are many time intervals with the same period t but with different starting and ending times to improve the ensemble sampling to get more accurate diffusional properties, the MSD as a function of t is obtained by averaging over all the squared displacements with the same time interval as indicated by the angular brackets in the expression.

The quantitative information on the diffusion of Li ions is implied by the slope of the MSD or the so-called tracer diffusion coefficient D_{tr} at a sufficient calculation time,

$$D_{\mathrm{tr}}(T) = \frac{1}{6} \lim_{t \to \infty} \frac{1}{(t - t_{\mathrm{eq}})} \mathrm{MSD}(t - t_{\mathrm{eq}}, T). \tag{11}$$

Here the subscript tr specifies the self-diffusion process for noninteracting Li ions.

By definition, the diffusion coefficient relates to the capacity of a Li ion to move a distance over a time interval, and such diffusive behavior is subjected to a thermally activated process, customarily we can describe this temperature-dependent diffusion coefficient in terms of an Arrhenius relationship analogous to the diffusion modeled by the NEB approach of Eq. (5),

$$D_{\mathrm{tr}}(T) = D_0 e^{-E_a^{\mathrm{MD}}/k_B T}, \tag{12}$$

where D_0 is a temperature-independent pre-exponential factor, k_B is the Boltzmann constant, and E_a^{MD} is the activation energy of motion which can be deduced from the Arrhenius plot of $\ln(D_{\mathrm{tr}}(T))$ versus $1/T$. In general, we expect that the activation energies deduced from the MD and the NEB analyses to differ because differing physical and mathematical approximations.

The ionic conductivity is related to the diffusion process via the Nernst-Einstein equation:

$$\sigma(T) = \rho q^2 \frac{D_{\mathrm{tr}}(T)}{k_B T H_r}. \tag{13}$$

Here $\rho = N_{\mathrm{Li}}/V$ denotes the ratio of the number of Li ions within the simulation cell to its volume V, q represents the charge of the Li ion (presumed to be $+1$, in units of the elementary charge unit e), H_r is the Haven ratio [58] which accounts for the effect of the correlation and collectivity effects of ionic motion. For our system, we take $H_r = 1$ with assumption of independent migrations of Li ions.

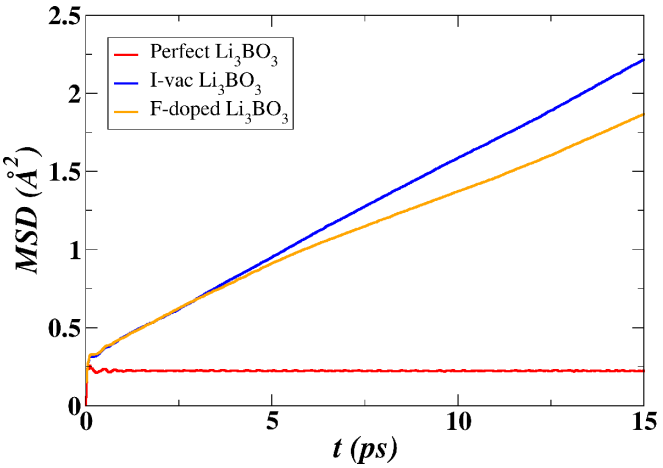

FIG. 6. Plots of $\mathrm{MSD}(t, \langle T \rangle)$ from Eq. (10) in units of Å^2 as a function of time in units of picoseconds for the stoichiometric, I-vac, and F-doped models of Li_3BO_3 at average temperatures of $\langle T \rangle =$ 968, 998, and 996 K, respectively.

A. Molecular dynamics simulations for Li_3BO_3

Results for the MSDs of Li ions in $3 \times 1 \times 1$ supercells of pure Li_3BO_3 as well as I-vac and F-doped models are presented in Fig. 6 for simulation temperatures of approximately 1000 K, evaluated according to Eq. (10). As the nearly horizontal MSD curve for pure Li_3BO_3 shows, the full ordering of Li ions in this material greatly limits their displacements, resulting in extremely low ionic mobility. It is expected that the Li ion mobility can be improved by introducing Li vacancies sites. In fact, this is seen in Fig. 6 in terms of the substantial slopes of the MSD curves for the I-vac and F-doped models.

To visualize the Li ion motions in the I-vac and F-doped models, in Fig. 7 we show the ball and stick diagrams for the initial B and O sites with superposed Li ion positions for the first 70 ps of the simulation with a time interval of 0.24 ps. The time sequence of the superposed images is missing from this visualization, however, it is clear that there is considerable motion of the Li ions during the course of the simulation. Interestingly, the pattern of superposed Li ion sites look very similar for the I-vac and F-doped models, each without obvious occupancy of interstitial sites. To the extent that there are a significant number of images between all of the host lattice Li sites, one can conclude that all of the Li ions [types Li (1), (2), and (3)] participate in ion migration, consistent with the predicted diffusion pathway in NEB calculations shown in Fig. 3. It is therefore encouraging and provides some confidence that the Li ion migrations in our simulated crystals are likely to occur via vacancy mechanisms.

Figure 8 summarizes the results for the Li ion conductivity of Li_3BO_3 versus $1000/T$. The calculated MD results were estimated using Eq. (13) with $H_r = 1$. In the present paper, the measurement of the ionic conductivity for the pure Li_3BO_3 with sample preparation described in Paper II [14]

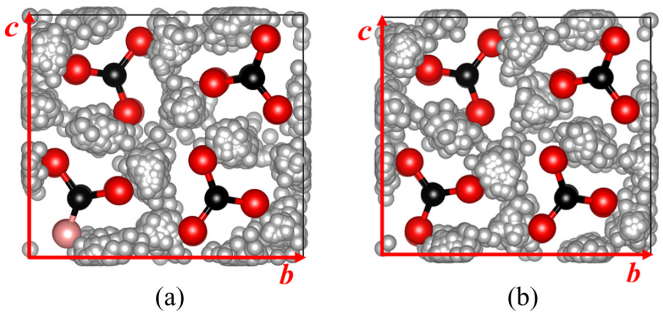

FIG. 7. Ball and stick diagrams of MD simulations for (a) I-vac Li_3BO_3 at temperature $\langle T \rangle = 996$ K and (b) F-doped Li_3BO_3 at temperature $\langle T \rangle = 998$ K. B, O, and F are shown at their initial positions with black red, and pink balls, respectively. Li positions of the initial configuration and 290 subsequent positions at time intervals of 0.24 ps are indicated with gray balls. Simulations were performed using microcanonical NVE ensembles in $3 \times 1 \times 1$ supercells. The diagram represents a projection onto the **bc** plane.

were conducted with gold blocking electrodes sputtering onto each side of the pellet sample for electrochemical impedance spectroscopy (EIS). EIS measurements were performed on a BioLogic SP-200 from 1 MHz to 100 MHz with an amplitude of 100 mV at temperatures ranging from $20 - 80\,^{\circ}$C. Figure 8 also includes the experimental data analyzed from the published work of Ohta *et al.* [15] and Shigeno *et al.* [31] using digitizing software. All the straight lines represent the linear fit of the discrete values, the slope of which determines the deduced activation energy based on the Nernst-Einstein and Arrhenius relationships given in Eqs. (13) and (12), as listed in Table V. It is interesting to note that the experimental measurements plotted here show a range of values that are roughly in the same range of the MD simulation results.

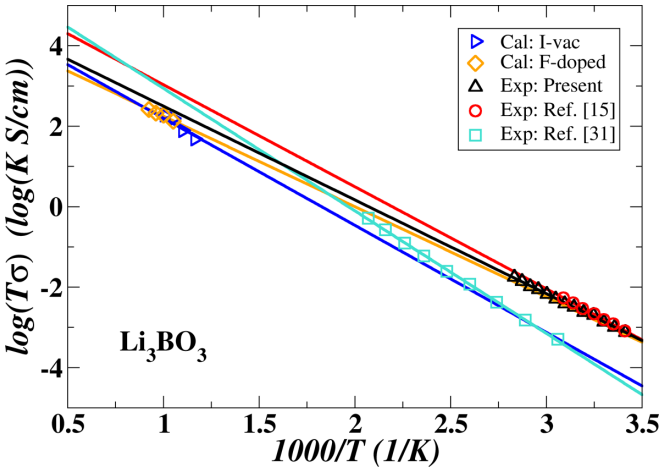

FIG. 8. Plot of computational and experimentally measured values of $\log_{10}(\sigma T)$ versus $1000/T$ for the I-vac and the F-doped models of Li_3BO_3. The computed values of σ were determined from Eq. (13). Lines represent least squares fits to the $\log_{10}(\sigma T)$ data. The experimental results for polycrystalline Li_3BO_3 (red circles) were obtained by refitting the data in Ref. [15] and for glassy Li_3BO_3 (green squares) were obtained by refitting the data in Ref. [31].

TABLE V. Results of activation energy on Li_3BO_3. The MD data in units of eV is determined from the slope of the straight line in Fig. 8, and the corresponding conductivity in units of S/cm is extrapolated to $T = 300$ K. The experimental results are listed as reported at $T = 25$ Celsius.

Material	Analysis	E_a	$\sigma(T = 300\,\text{K})$
I-vac Li_3BO_3	MD	0.53	3.2×10^{-7}
	NEB	0.38	–
F-doped Li_3BO_3	MD	0.45	3.4×10^{-6}
	NEB	0.72	–
Polycrystalline Li_3BO_3	Exp[a]	0.46	3.8×10^{-6}
Polycrystalline Li_3BO_3	Exp[b]	0.51	2.0×10^{-6}
Glassy Li_3BO_3	Exp[c]	0.60	3.4×10^{-7}

[a]The present experimental measurement.
[b]Experimental data from Ref. [15].
[c]Experimental data from Ref. [31].

In Table V, we list the results of NEB and MD simulations together with the experimental measurements. The larger estimated room-temperature conductivity and slightly lower activation energy of the F-doped Li_3BO_3 relative to the I-vac Li_3BO_3 suggests that substitutional doping of O with F creates an enabling environment for Li ion migration processes. While due to the trapping effect, the NEB results on the F-doped Li_3BO_3 are strongly influenced by the Li ion hops near the F site. The more physical picture is expected to be provided by MD simulations with an effective barrier evaluated over the hopping events of all mobile Li ions. The simulations on crystals with Li vacancies and the fitted results from the experiment shows good agreement, particularly the room-temperature conductivities of the calculated value and the experimental measurement are in the same order of magnitude $10^{-7} - 10^{-6}$ S/cm. Although our experimental measurements on the phase-pure Li_3BO_3 and the experimental papers [15,31] do not mention intentional doping in their sample preparation, the simulation results suggest that vacancy populations are likely to be present in the current experimental samples and the samples reported in Refs. [15,31] as well. This speculation is motivated both by the MD simulations near $T = 1000$ K, showing negligible Li MSDs for simulations on initially perfect configurations in contrast to simulations on initial configurations containing a single vacancy in the supercell shown in Fig. 6, and by the estimate of the interstitial-vacancy pair energy of $E_f = 1.25$ eV for this system. These results suggest that, while the bottleneck for vacancy formation is too high to generate conductivity in an ideal crystal, perhaps a small number of such Frenkel defects are typically formed during synthesis of these materials.

B. Molecular dynamics simulations for Li_3BN_2

To explore the performance of Li_3BN_2 as an ionic conductor, in Fig. 9 we plot the MSDs as a function of simulation time for MD simulations at average temperatures near 1300 K. Here we compare models of stoichiometric Li_3BN_2 having fully occupied host sites in the initial configuration, with the I-int model initially having an extra Li at one of the

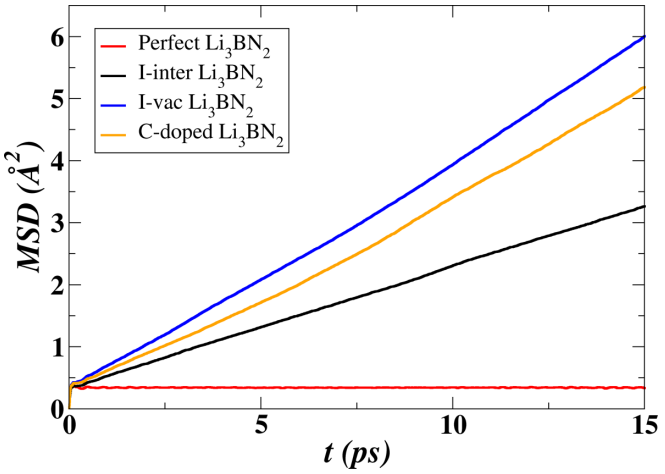

FIG. 9. Plots of MSD(t, $\langle T \rangle$) from Eq. (10) in units of Å^2 as a function of time in units of picosecond for $2 \times 2 \times 1$ supercells of Li_3BN_2 for the stoichiometric, I-int, I-vac, and C-doped models at average temperatures of $\langle T \rangle = 1272, 1259, 1254$, and 1261 K, respectively.

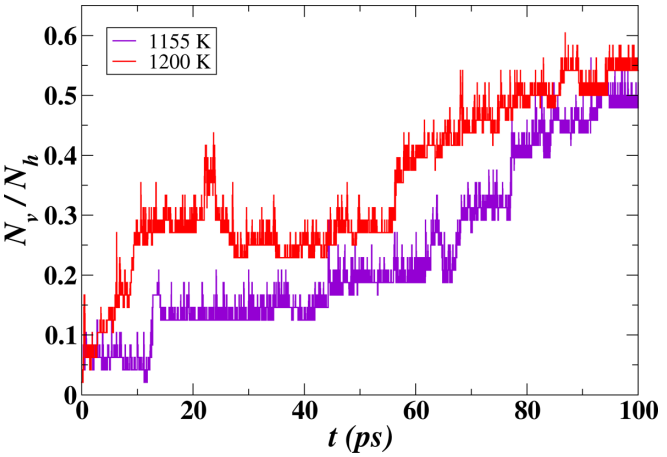

FIG. 10. Plots of fractions of vacancies with respect to simulation time in units of picosecond for I-vac Li_3BN_2 at $\langle T \rangle = 1155$ K (purple) and 1200 K (red).

metastable interstitial sites, with the I-vac model initially having a missing Li ion, and the C-doped model having a C ion substituting for one B ion together with a missing Li ion. For the C-doped models, we observed that the N–C–N bond is robust; showing no evidence of breaking throughout the simulation at each considered temperature. From the figure, we see that the Li ions of the stoichiometric model present trivial displacements with a flat MSD curve, indicating very high activation energy for triggering the diffusion process. By contrast, the three different defect configurations display measurable diffusivity with comparable slopes for a similar temperature. For the I-int model, we found that the interstitial Li ion only jumps back and forth between adjacent interstitial sites, causing a very localized and short-ranged migration in terms of a pure interstitial mechanism. Consistent with the kick-out process discussed above using the NEB analysis, the vacancy mechanism is found to be significant for the I-int model. For these high temperature simulations, it is interesting that the MSD curves predict that diffusivity of the I-vac model to be almost twice that of the I-int model, with the C-doped model predicted to have a diffusivity in between but more similar to that of the I-vac model.

To examine the role of Li ion vacancies in determining ion mobility, we can follow the Li ion trajectories $\mathbf{R}_i(t)$ to estimate the fraction of vacancy sites at any given time step t. For our constant volume simulations of the $2 \times 2 \times 1$ supercell, the location of each of the $N_h = 48$ host lattice sites are known. They are analyzed as occupied at time t if a Li ion is found within 1 Å of the site; otherwise it is vacant. In this way, the number of vacancies at each time step $N_v(t)$ and the ratio $N_v(t)/N_h$ can be calculated. Not surprisingly, the vacancy ratio increases over time and with temperature. An example of vacancy fraction analysis for the I-vac model at two different temperatures is shown in Fig. 10. Similar results were obtained from the C-doped model. Here we see that at these temperatures, the vacancy fraction steadily rises, increasing more rapidly at the higher temperature. In each case, we found that the most of the Li ions leaving the normal host sites did not hop into the interstitial defect positions but tended to hover at the intermediate sites between the host sites that constitute the main vacancy conducting path. On one hand, because of the growing number of unoccupied host sites as time progresses, the structure becomes increasingly defective and disordered, which may promote the ion diffusion. On the other hand, as suggested by Fig. 4 of the NEB analysis, the single hop barrier energies between neighboring host sites are unevenly distributed with relatively high values, thus slowing down the conduction of Li ions even with considerable vacant sites available to be occupied.

Using a similar approach to quantify the time-dependent occupancy of interstitial sites finds that the interstitial sites

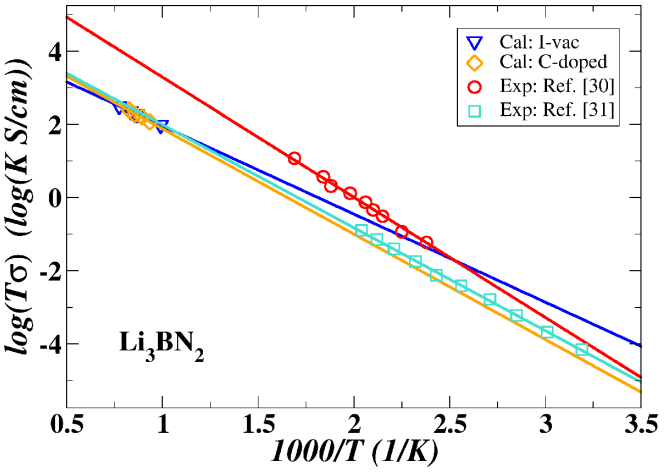

FIG. 11. Plots of $\log_{10}(\sigma T)$ vs $1000/T$ for the I-vac Li_3BN_2 (blue) and the C-doped Li_3BN_2 (orange). The data points were gathered from MD simulations and the straight line is a linear fit of the points with the slope determining the activation energy. The experimental results for polycrystalline Li_3BN_2 (red circles) were obtained by refitting the data in Ref. [30] and for glass-ceramic Li_3BN_2 (green squares) were obtained by refitting the data in Ref. [31].

TABLE VI. Results of conductivity simulations in comparison with the available experimental data. Energies are given in eV and the ionic conductivities are in units of S/cm. The experimental conductivities are listed as reported at (or extrapolated to) $T = 25$ Celsius.

Materials	Analysis	E_a	$\sigma(T = 300\,\mathrm{K})$
I-vac Li_3BN_2	MD	0.48	7.2×10^{-7}
	NEB	0.30 (**a**)/0.81 (**bc**)	–
C-doped Li_3BN_2	MD	0.57	4.8×10^{-8}
	NEB	0.40 (**a**)/1.02 (**bc**)	–
Polycrystalline Li_3BN_2	Exp[a]	0.66	1.4×10^{-7}
Glass-ceramic Li_3BN_2	Exp[b]	0.56	1.1×10^{-7}

[a]Experimental data from Ref. [30].
[b]Experimental data from Ref. [31].

are found to play a minor role in the Li ion mobility in these systems.

From this insight, we focus on studying the ionic conductivity for the I-vac and C-dopped models of Li_3BN_2 using Eq. (13) with $H_r = 1$ to analyze MD simulations with average temperatures ranging between $1000 - 1300$ K. The results are shown in Fig. 11. The experimental data were analyzed from the published work of Yamane *et al.* [30] and Shigeno *et al.* [31] using digitizing software. The Li ion activation energies, as listed in Table VI, are deduced from the slopes of the linear fit lines of the discrete values according to the Nernst-Einstein and Arrhenius relationships given in Eqs. (13) and (12). It is also noticeable that the plots of the experimental measurements and the MD simulations are in the same range of values over the explored temperature range.

According to the results listed in Table VI, the activation energy for the C-doped model is 0.57 eV compared to 0.48 eV for the I-vac model. In general, the calculated MD results for the activation energy and room-temperature ionic conductivity are comparable with the experimental measurements. Following the MD trajectories, we find that the first diffusion channel formed in each structure is along the **a** axis, consisting of the most energetically favorable path identified in NEB calculations. Also, it is reasonable to see that for each model, the calculated activation energy from MD simulations falls in between the NEB data of the lowest barrier channel along the **a** axis and the NEB results of **bc** plane in which the massive Li ion diffusions are less likely to occur.

VI. SUMMARY AND CONCLUSIONS

Using NEB methods and MD simulations, we have studied the Li ion migration mechanisms of crystalline Li_3BO_3 and Li_3BN_2, both having monoclinic structure with space group symmetry $P2_1/c$. The two materials were found to be similar in terms of the Li ions positioning themselves within BO_3^{3-} or BN_2^{3-} anion frameworks as well as their Li ion conductivity mechanisms being characterized by vacancy processes. For both materials, the NEB analysis was able to identify the main Li ion vacancy migration pathways which turned out to be qualitatively consistent with the MD trajectories such as shown in Fig. 7 for Li_3BO_3. For Li_3BO_3, the migration path is two-dimensional within the **bc** plane, involving all of the Li ion sites. By contrast, the migration is one-dimensional along the **a** axis for Li_3BN_2, involving only Li ion sites of type Li(1). In addition, the MD simulations show the Li ion to spend a significant amount of its time at a distance of more than 1 Å away from its equilibrium host site. This is shown qualitatively in Fig. 7 for Li_3BO_3 and more quantitively in Fig. 10 for Li_3BN_2.

Using MSD analysis of the MD results and approximating the Haven ratio to be 1, the ionic conductivity could be calculated from Eq. (13). The results for Li_3BO_3 shown in Fig. 8 and the results for Li_3BN_2 shown in Fig. 11 suggest very similar outcomes for simulations using supercells with an ideal vacancy or a vacancy due to substitutional doping. Moreover, simulation for both materials at high temperature extrapolate with respect to $1000/T$ to values that are close to data available from experimental measurements, including measurements on Li_3BO_3 generated for this paper. The Li ion conductivity at 300 K is $10^{-7} - 10^{-6}$ S/cm for Li_3BO_3 and $10^{-8} - 10^{-7}$ S/cm for Li_3BN_2. It is interesting to speculate about possible sources of Li ion vacancies needed for the conduction processes in the experimental samples since these were prepared without intentional doping. One possibility might be that stable vacancy-interstitial defect pairs, usually known as Frenkel defects, are present in these samples. Our simulations show that while perfect crystals exhibit no conductivity, simulations with a Li vacancy ratio of 1/12 for Li_3BO_3 and 1/16 for Li_3BN_2 show reasonable agreement with the experiment.

ACKNOWLEDGMENTS

This work was supported by NSF Grant No. DMR-1940324. Computations were performed on the Wake Forest University DEAC cluster, a centrally managed resource with support provided in part by the university. Z.D.H. was supported by Laboratory Directed Research and Development (LDRD) funding from Argonne National Laboratory, provided by the Director, Office of Science, of the U.S. Department of Energy under Contract No. DE-AC02-06CH11357.

[1] D. Campanella, D. Belanger, and A. Paolella, J. Power Sources **482**, 228949 (2021).
[2] M. Balaish, J. C. Gonzalez-Rosillo, K. J. Kim, Y. Zhu, Z. D. Hood, and J. L. M. Rupp, Nat. Energy **6**, 227 (2021).
[3] Y. Zhu, J. C. Gonzalez-Rosillo, M. Balaish, Z. D. Hood, K. J. Kim, and J. L. M. Rupp, Nat. Rev. Mater. **6**, 313 (2020).
[4] K. J. Kim, M. Balaish, M. Wadaguchi, L. Kong, and J. L. M. Rupp, Adv. Energy Mater. **11**, 2002689 (2020).
[5] M. V. Reddy, C. M. Julien, A. Mauger, and K. Zaghib, Nanomaterials **10**, 1606 (2020).
[6] M. M. Ioanniti, F. Hu, and W. E. Tenhaeff, J. Vac. Sci. Technol. A **38**, 060801 (2020).

[7] X. Miao, H. Wang, R. Sun, C. Wang, Z. Zhang, Z. Li, and L. Yin, Energy Environ. Sci. **13**, 3780 (2020).

[8] Z. Tong, S.-B. Wang, Y.-K. Liao, S.-F. Hu, and R.-S. Liu, ACS Appl. Mater. Interfaces **12**, 47181 (2020).

[9] J. Li, C. Ma, M. Chi, C. Liang, and N. J. Dudney, Adv. Energy Mater. **5**, 1401408 (2015).

[10] W. C. West, Z. D. Hood, S. P. Adhikari, C. Liang, A. Lachgar, M. Motoyama, and Y. Iriyama, J. Power Sources **312**, 116 (2016).

[11] Y. Zhu, X. He, and Y. Mo, Adv. Sci. **4**, 1600517 (2017).

[12] Z. D. Hood, X. Chen, R. L. Sacci, X. Liu, G. M. Veith, Y. Mo, J. Niu, N. J. Dudney, and M. Chi, Nano Lett. **21**, 151 (2021).

[13] W. D. Richards, L. J. Miara, Y. Wang, J. C. Kim, and G. Ceder, Chem. Mater. **28**, 266 (2016).

[14] Y. Li, Z. D. Hood, and N. A. W. Holzwarth, Phys. Rev. Materials **5**, 085403 (2021).

[15] S. Ohta, S. Komagata, J. Seki, T. Saeki, S. Morishita, and T. Asaoka, J. Power Sources **238**, 53 (2013).

[16] M. He, H. Okudera, J. Fleig, A. Simon, X. Chen, and J. Maier, J. Solid State Chem. **178**, 680 (2005).

[17] H. Yamada, J. Indian Inst. Sci. **96**, 315 (2016).

[18] M. Tatsumisago, R. Takano, K. Tadanaga, and A. Hayashi, J. Power Sources **270**, 603 (2014).

[19] M. Eom, S. Choi, S. Son, L. Choi, C. Park, and D. Shin, J. Power Sources **331**, 26 (2016).

[20] K. Nagao, A. Hayashi, and M. Tatsumisago, J. Ceram. Soc. Jpn. **124**, 915 (2016).

[21] K. Nagao, M. Nose, A. Kato, A. Sakuda, A. Hayashi, and M. Tatsumisago, Solid State Ionics **308**, 68 (2017).

[22] M. Tatsumisago, R. Takano, M. Nose, K. Nagao, A. Kato, A. Sakuda, K. Tadanaga, and A. Hayashi, J. Ceram. Soc. Jpn. **125**, 433 (2017).

[23] K. Nagao, A. Sakuda, A. Hayashi, and M. Tatsumisago, J. Power Sources **424**, 215 (2019).

[24] H. W. Langmi and G. S. McGrady, J. Alloys Compd. **466**, 287 (2008).

[25] H. Yamane, T. Kano, A. Kamegawa, M. Shibata, T. Yamada, M. Okada, and M. Shimada, J. Alloys Compd. **402**, L1 (2005).

[26] M. Kagamida, H. Kanda, M. Akaishi, A. Nukui, T. Osawa, and S. Yamaoka, J. Cryst. Growth **94**, 261 (1989).

[27] S. Nakano, H. Ikawa, and O. Fukunaga, Diamond Relat. Mater. **3**, 75 (1993).

[28] O. Fukunaga and S. Takeuchi, Int. J. Refract. Met. Hard Mater. **55**, 54 (2016).

[29] S. Emani, C. Liu, M. Ashuri, K. Sahni, J. Wu, W. Yang, K. Németh, and L. L. Shaw, ChemElectroChem **6**, 320 (2019).

[30] H. Yamane, S. Kikkawa, and M. Koizumi, J. Solid State Chem. **71**, 1 (1987).

[31] M. Shigeno, K. Nagao, M. Deguchi, C. Hotehama, H. Kowada, A. Sakuda, A. Hayashi, and M. Tatsumisago, Solid State Ionics **339**, 114985 (2019).

[32] *International Tables for Crystallography, Volume A: Space-Group Symmetry,*5th revised ed., edited by T. Hahn (Kluwer Academic Publishers, Boston, 2002).

[33] M. I. Aroyo, J. M. Perez-Mato, D. Orobengoa, E. Tasci, G. De La Flor, and A. Kirov, Bulg. Chem. Commun. **43**, 183 (2011), http://www.cryst.ehu.es/.

[34] H. Jónsson, G. Mills, and K. W. Jacobsen, in *Classical and Quantum Dynamics in Condensed Phase Simulations*, edited by B. J. Berne, G. Ciccotti, and D. F. Coker (World Scientific, Singapore, 1998), pp. 385–404.

[35] G. Henkelman, B. P. Uberuaga, and H. Jónsson, J. Chem. Phys. **113**, 9901 (2000).

[36] G. Henkelman and H. Jónsson, J. Chem. Phys. **113**, 9978 (2000).

[37] P. Hohenberg and W. Kohn, Phys. Rev. **136**, B864 (1964).

[38] W. Kohn and L. J. Sham, Phys. Rev. **140**, A1133 (1965).

[39] P. E. Blöchl, Phys. Rev. B **50**, 17953 (1994).

[40] N. A. W. Holzwarth, A. R. Tackett, and G. E. Matthews, Comput. Phys. Commun. **135**, 329 (2001), http://pwpaw.wfu.edu.

[41] P. Giannozzi, O. Andreussi, T. Brumme, O. Bunau, M. Buongiorno Nardelli, M. Calandra, R. Car, C. Cavazzoni, D. Ceresoli, M. Cococcioni, N. Colonna, I. Carnimeo, A. Dal Corso, S. de Gironcoli, P. Delugas, R. A. DiStasio, A. Ferretti *et al.*, and J. Phys.: Condens. Matter **29**, 465901 (2017), http://www.quantum-espresso.org.

[42] P. Giannozzi, O. Baseggio, P. Bonfà, D. Brunato, R. Car, I. Carnimeo, C. Cavazzoni, S. de Gironcoli, P. Delugas, F. Ferrari Ruffino, A. Ferretti, N. Marzari, I. Timrov, A. Urru, and S. Baroni, J. Chem. Phys. **152**, 154105 (2020), http://quantumespresso.org.

[43] J. P. Perdew, A. Ruzsinszky, G. I. Csonka, O. A. Vydrov, G. E. Scuseria, L. A. Constantin, X. Zhou, and K. Burke, Phys. Rev. Lett. **100**, 136406 (2008).

[44] K. Momma and F. Izumi, Appl. Crystallogr. **44**, 1272 (2011), code available from http://jp-minerals.org/vesta/en/.

[45] A. Kokalj, Comput. Mater. Sci. **28**, 155 (2003), code available at http://www.xcrysden.org.

[46] Y.-W. Hu, I. D. Raistrick, and R. A. Huggins, J. Electrochem. Soc. **124**, 1240 (1977).

[47] V. Thangadurai and W. Weppner, Ionics **8**, 281 (2002).

[48] J. C. Bachman, S. Muy, A. Grimaud, H.-H. Chang, N. Pour, S. F. Lux, O. Paschos, F. Maglia, S. Lupart, P. Lamp, L. Giordano, and Y. Shao-Horn, Chem. Rev. **116**, 140 (2016).

[49] E. Kazyak, K.-H. Chen, A. L. Davis, S. Yu, A. J. Sanchez, J. Lasso, A. R. Bielinski, T. Thompson, J. Sakamoto, D. J. Siegel, and N. P. Dasgupta, J. Mater. Chem. A **6**, 19425 (2018).

[50] S. H. Jung, K. Oh, Y. J. Nam, D. Y. Oh, P. Brüner, K. Kang, and Y. S. Jung, Chem. Mater. **30**, 8190 (2018).

[51] N. D. Lepley and N. A. W. Holzwarth, J. Electrochem. Soc. **159**, A538 (2012).

[52] M. G. Down, M. J. Haley, P. Hubberstey, R. J. Pulham, and A. E. Thunder, J. Chem. Soc. Dalton Trans. 1407(10) (1978).

[53] In principle, both vacancy and interstitial defects can be analyzed in this way. However, in the present paper, multiple vacancy defect and single interstitial defect configurations were considered for each system.

[54] A. R. West, *Basic Solid State Chemistry*, 2nd ed. (John Wiley & Sons, Ltd., Hoboken, NJ, 1999).

[55] W. D. Swope, H. C. Andersen, P. H. Berens, and K. R. Wilson, J. Chem. Phys. **76**, 637 (1982).

[56] J. D. Howard and N. Holzwarth, Solid State Ionics **325**, 80 (2018).

[57] X. He, Y. Zhu, A. Epstein, and Y. Mo, npj Comput. Mater. **4**, 18 (2018).

[58] Y. Haven and B. Verkerk, Phys. Chem. Glasses **6**, 38 (1965).